AIAA JOURNAL
Vol. 46, No. 10, October 2008

Multiple Sound Generation in Interaction of Shock Wave with Strong Vortex

A. Chatterjee*
Gyeongsang National University, Jinju 660-701, Republic of Korea
and
S. Vijayaraj†
Indian Institute of Technology, Bombay, Mumbai 400 076, India

DOI: 10.2514/1.36050

The interaction between an initially planar shock wave and a strong vortex is numerically simulated in a relatively large computational domain for long simulation times. A numerical scheme of very-high-order spatial accuracy is used. Multiple acoustic waves, quadrupolar in nature and successively out of phase, are captured in the numerical simulations. The number of acoustic waves captured are more than the maximum of three previously reported in literature in the interaction of an initially planar shock wave with a compressible vortex. The additional sound waves observed are due to acoustic radiation from the rotating elliptical vortex following the interaction of the incident shock wave and the initially circular vortex.

I. Introduction

SHOCK–TURBULENCE interaction is a major contributor to the phenomenon of aerodynamic noise in supersonic jets. This interaction is often studied using a simplified model that has an initially planar shock wave interacting with a single isolated vortex. Early efforts to study this simplified interaction were experimental in nature and involved a columnar vortex interacting with a planar shock wave. The acoustic wave generated in such an interaction is seen to be cylindrical and centered around the vortex downstream of the shock wave. These experiments also revealed the circumferential pressure distribution of the resulting acoustic wave to be quadrupolar, consisting of four alternate compression and expansion regions. The linear theory developed by Ribner [1] to model this interaction predicted the occurrence of a precursor wave followed by an acoustic wave. Both of the resulting waves are shown to have a quadrupolar distribution and to be out of phase. Subsequent efforts to study the problem tended to be more computational in nature and involved solving the two-dimensional compressible unsteady Euler or Navier–Stokes equations. Computations were mostly directed toward strong shock–vortex interactions with significant shock deformation. This deformation can also result in the formation of secondary or reflected shock structures. Numerical simulations of shock–vortex interactions by Ellzey et al. [2] confirmed the presence of two sound waves, quadrupolar in nature and out of phase. These computations involving strong shock–vortex interactions also pointed to the role played by secondary or reflected shock structures to the sound wave generation process. Reflected shock waves were seen to merge with the quadrupolar pressure variation of the generated acoustic waves, forming stronger compressive regions than predicted by linear theory. Partly based on the presence of these reflected shock waves, Inoue and Hattori [3] predicted a third sound wave to be generated in the interaction of an initially planar shock wave and a single vortex. Subsequent numerical simulations [4,5] involving a relatively larger physical domain and simulation time revealed the presence of a third sound wave. Rault et al. [6] observed that a stronger vortex in the shock–vortex interaction process leads to an earlier appearance of the third sound wave. Zhang et al. [7] conducted an extensive numerical study of the interaction of a planar shock wave with a strong vortex. Their numerical study describes the multistage feature in shock–vortex interactions involving a strong vortex. Reflected or secondary shock waves generated in the primary or first-stage interaction are shown to interact with the deformed vortex. These secondary interactions result in the production of shocklets. The shocklets, in turn, interact with the deformed vortex, causing tertiary or third-stage interactions. However, in their numerical simulations, Zhang et al. were able to capture only three sound waves attributed to the first-stage of the multistage strong vortex-shock interaction process. Zhang et al. commented on the possibility of additional sound waves being generated in the subsequent secondary (and tertiary) interactions involving reflected shocks, shocklets, and the deformed vortex. A limited domain size and small simulation time has been cited as the possible reason for not being able to capture these additional suspected sound waves. Inoue [4] observed additional acoustic waves to be generated by secondary interactions in numerical simulations involving a shock wave and two vortices. These secondary interactions had reflected shock waves, formed in the interaction of the incident shock with one vortex, interacting with the second vortex. However, generation of more than three acoustic waves in an interaction involving an initially planar shock wave and a single vortex has not been reported in literature. This is true irrespective of the relative strengths of the shock and the vortex.

In the present work, the interaction between an initially planar shock wave and a strong vortex is numerically simulated in a relatively large computational domain for long simulation times. Numerical schemes of very-high-order spatial accuracy are employed. Shock and vortex strengths are chosen so that the shock–vortex interaction process exhibits a multistage feature. This feature is assumed to signify an interaction between a shock wave and a strong vortex. Multiple acoustic waves, in addition to the usual three, are captured in the present numerical simulations. The additional sound waves generated are quadrupolar in nature and successively out of phase, similar to that attributed to the primary shock–vortex interaction in literature. Results rule out the possibility that extra acoustic waves captured are generated due to secondary (or tertiary) interactions between additionally generated shock structures and the deformed vortex. The shock–vortex interaction

Received 6 December 2007; revision received 25 June 2008; accepted for publication 26 June 2008.

*Visiting Research Professor, Research Center for Aircraft Parts Technology, School of Mechanical and Aerospace Engineering; currently Associate Professor, Department of Aerospace Engineering, Indian Institute of Technology, Bombay, Mumbai 400 076, India; avijit@aero.iitb.ac.in.

†Graduate Student, Department of Aerospace Engineering; vijayaraj@aero.iitb.ac.in.

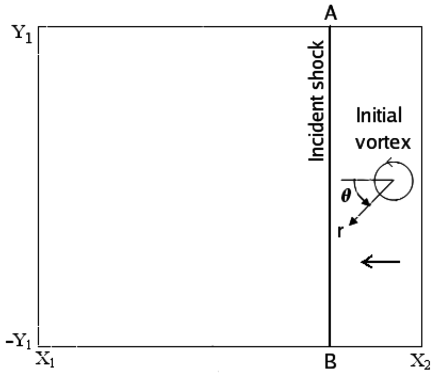

Fig. 1 Computational domain.

compresses the initially circular vortex into an elliptical shape that rotates and radiates acoustic waves like a rotating quadrupole. Additional acoustic waves are seen for shock–vortex interactions with shock and vortex strengths that coincidentally also exhibit a multistage feature. Shock–vortex interactions involving a weaker vortex do not exhibit significant rotation for the elliptical vortex at later times. Such interactions also do not result in the generation of additional sound waves. Ellzey and Henneke [8] have shown the importance of both shock distortion and vortex compression for the generation of quadrupolar acoustic waves in shock–vortex interactions. They also showed vortex compression to be the dominant mechanism in the generation of quadrupolar acoustic wave for interactions with small shock distortion. Present results indicate the rotating elliptical vortex resulting from a strong vortex-shock interaction to be the source of quadrupolar acoustic waves following cessation of both shock distortion and shock-induced vortex compression.

II. Numerical Technique

Shock–vortex interactions in the present work are simulated by solving the two-dimensional unsteady Euler equations of gas dynamics. Inoue and Hattori [3] have shown the effect of Reynolds number to be negligibly small for such problems. This is attributed to the much larger viscous dissipation time compared with other relevant time scales present in the problem [2]. Ninth-order weighted essentially nonoscillatory (WENO) [9,10] schemes are used for the space discretization, and advancement in time is through a fourth-order Runge–Kutta time stepping. WENO schemes are extensions of essentially nonoscillatory (ENO) [11] schemes, which allow higher-order accuracy in smooth parts of the solution along with sharp nonoscillatory representation of shock waves. ENO schemes approximate the numerical flux by choosing the smoothest stencil from a set of candidate stencils. The simultaneous capability of ENO schemes for higher-order accuracy and nonoscillatory resolution of shock waves is especially desirable for problems containing both strong shocks and complicated smooth flow structures [12,13]. The strong shock–vortex interaction is a good example of such a problem and provides an ideal setting for the use of the higher-order ENO and WENO schemes in literature [7,13–15]. WENO schemes extend the accuracy of ENO schemes in smooth regions of the flow by approximating the numerical flux using a convex combination of all the ENO candidate stencils [9]. The superiority of the ninth-order WENO scheme over a lower-order (fifth-order) WENO scheme in resolving flowfields containing both shock waves and complex flow features is demonstrated in [16]. The ninth-order WENO scheme in the present work is identical to that used for the demonstration in [16].

A. Initial and Boundary Conditions

The computational domain is rectangular in nature ($x_1 \le x \le x_2$ and $-y_1 \le y \le y_1$) as shown in Fig. 1. The shock wave is fixed at $x = 0$ and the vortex is located initially at $(x_v, 0)$. The vortex moves

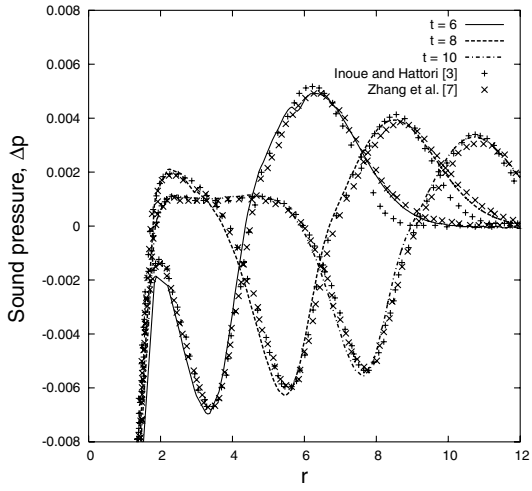

a)

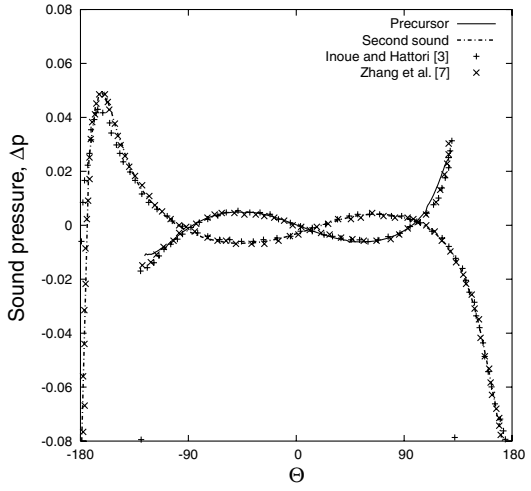

b)

Fig. 2 Validation results for $M_s = 1.2$ and $M_v = 0.25$: a) radial distribution $\Theta = -45$ deg and b) circumferential distribution $t = 6$ (ninth-order WENO scheme, 640 × 640 grid).

right to left with respect to the shock wave. The initial vortex is identical to that in [3,7] with tangential velocity $u_\theta(r) = M_v r e^{(1-r^2)/2}$, radial velocity $u_r = 0$, pressure

$$p(r) = \frac{1}{\gamma}\left(1 - \frac{\gamma - 1}{2} M_v^2 e^{1-r^2}\right)^{\gamma/(\gamma-1)}$$

and density

$$\rho(r) = \left(1 - \frac{\gamma - 1}{2} M_v^2 e^{1-r^2}\right)^{1/(\gamma-1)}$$

where $\gamma = 1.4$ is the specific heat ratio, $M_v = u_{\theta\max}/a_\infty$ is the vortex Mach number based on the maximum tangential velocity $u_{\theta\max}$, and a_∞ the speed of sound upstream of the shock wave. The shock wave Mach number $M_s = u_\infty/a_\infty$, with u_∞ being the supersonic flow

Table 1 Shock wave and vortex Mach numbers for numerical simulations

Cases	M_s	M_v
A	1.2	1.0
B	1.3	1.0
C	1.1	1.0
D	1.2	1.1
E	1.2	0.9

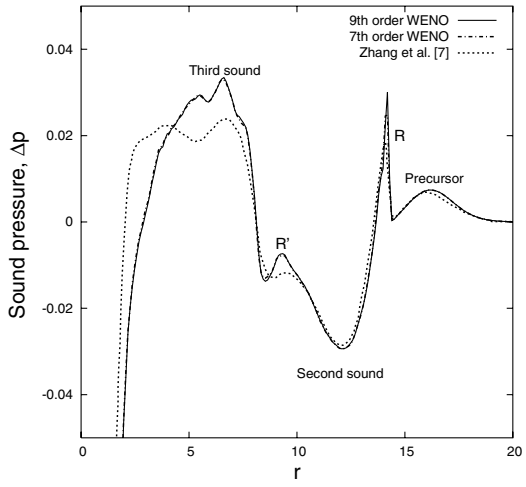

a)

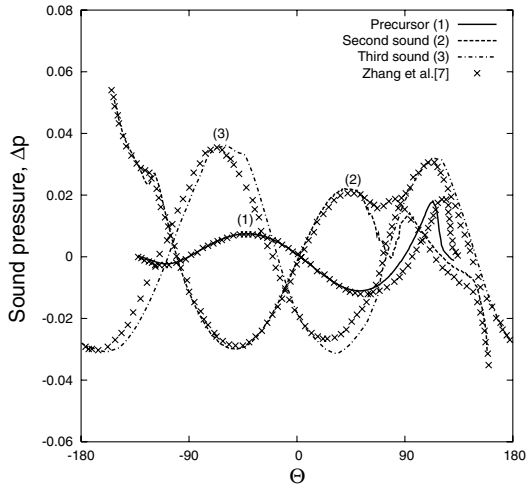

b)

Fig. 3 Results at $t = 16$ showing the third sound wave: a) radial distribution $\Theta = -45$ deg and b) circumferential distribution (ninth-order WENO scheme).

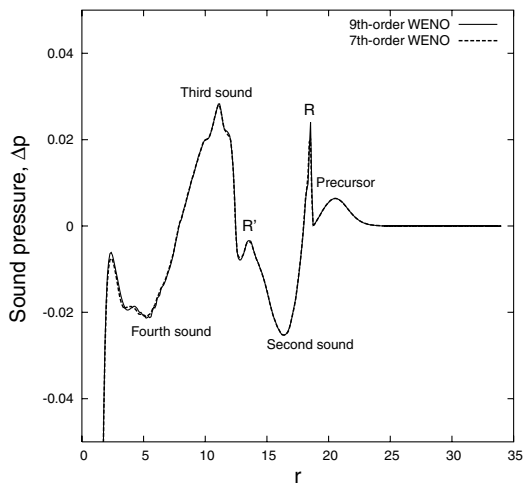

a)

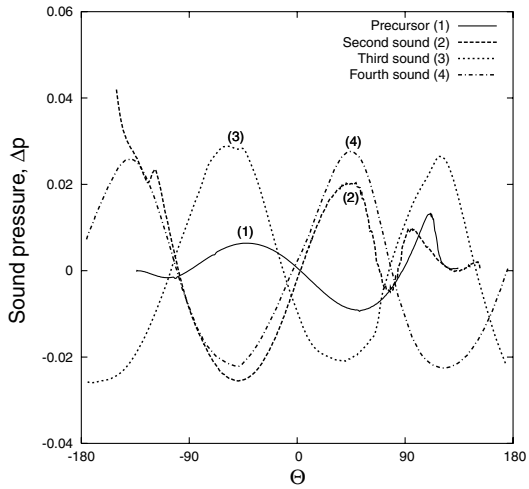

b)

Fig. 4 Results at $t = 20$ showing the fourth sound wave: a) radial distribution $\Theta = -45$ deg and b) circumferential distribution (ninth-order WENO scheme).

velocity upstream of the shock wave. The effect of the vortex is initially negligible beyond $r = 4$ from the vortex center, and this can be considered to be the basic length scale in the problem. The computational domain in the present work has the downstream boundary $x_1 = -70$ and upstream boundary $x_2 = 10$, and the upper and lower boundaries are defined by $y_1 = 40$. The initial vortex position is given by $x_v = 4$. The size of the computational domain is an important factor in the present analysis and is discussed in the next section. Periodic boundary conditions are imposed on the top and bottom boundaries. Nonreflecting boundary conditions are applied at the subsonic outflow boundary downstream of the shock wave. Flow conditions are held fixed at the supersonic inflow. The shock–vortex interaction results are initially validated for a test case corresponding to $M_s = 1.2$ and $M_v = 0.25$, as was also carried out in [7]. Figures 2a and 2b, respectively, compare the present radial and circumferential sound pressure distributions at different time t with computational results of Inoue and Hattori [3] and Zhang et al. [7]. Good agreement can be seen between these results. As in previous works [3,5,7], time is nondimensionalized using the vortex core radius and speed of sound upstream of the shock wave. The sound pressure Δp is defined as $(p - p_s)/p_s$ where p_s is the pressure behind the shock wave.

B. Test Cases and Computational Domain

The test cases solved for are listed in Table 1 in terms of shock wave Mach number M_s and vortex Mach number M_v. The test cases consider an initially planar shock wave interacting with a strong vortex. In the present context, a strong vortex is defined as one that ensures a multistage feature in the shock–vortex interaction [7]. The multistage feature results in additionally generated shock structures interacting with the deformed vortex and is assumed to signify an interaction between an incident shock wave and a strong vortex. Case A in Table 1 has been extensively studied in [7] to bring out the multistage feature in the interaction of a shock wave with a strong vortex. Other test cases listed in Table 1 are obtained by making relatively modest changes to values for M_s and M_v in case A, so that the multistage feature of the interaction is preserved. The extent of the computational domain and the total simulation time in the present work is based on case A.

The two-dimensional Navier–Stokes simulations of Zhang et al. [7] for the interaction of a shock wave with a strong vortex used a spatially fifth-order-accurate WENO discretization and a third-order Runge–Kutta time advancement. The domain size considered was 40×40 and consisted of 1280×960 grid points; simulations were carried out until $t = 16$. Inoue's [4] numerical simulations involving a relatively weaker vortex were performed on a much larger domain measuring approximately 88×96. A sixth-order compact Pade scheme was used to solve the two-dimensional Navier–Stokes equations. The discretization consisted of 1070×1128 grids points with results reported until $t = 40$. However, as in [7], only three acoustic waves were confirmed in the simulations. Some additional pressure peaks were observed for the strongest interaction ($M_s = 1.2$ and $M_v = 0.5$) simulated. Earlier studies [6] have indicated that increasing M_v decreases the simulation time required for the appearance of the third sound wave. Thus, it is possible that the larger

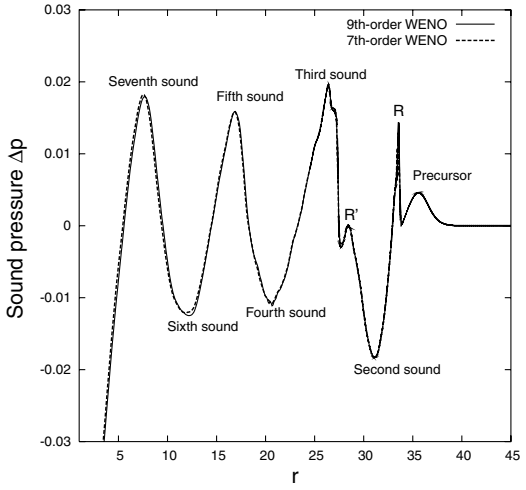

a)

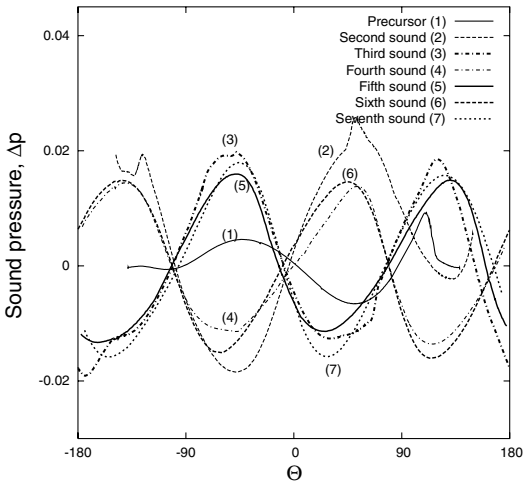

b)

Fig. 5 Results at $t = 34$ showing the seven sound waves: a) radial distribution $\Theta = -45$ deg and b) circumferential distribution (ninth-order WENO scheme).

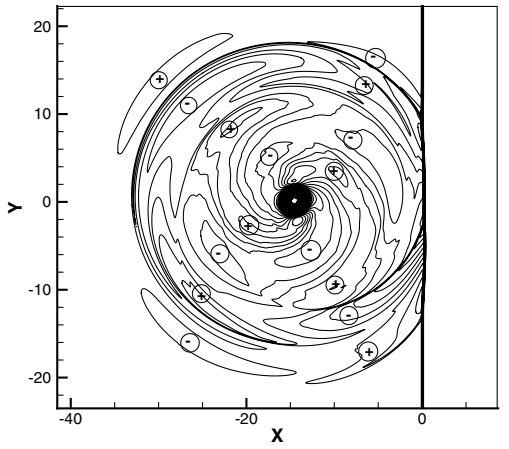

a)

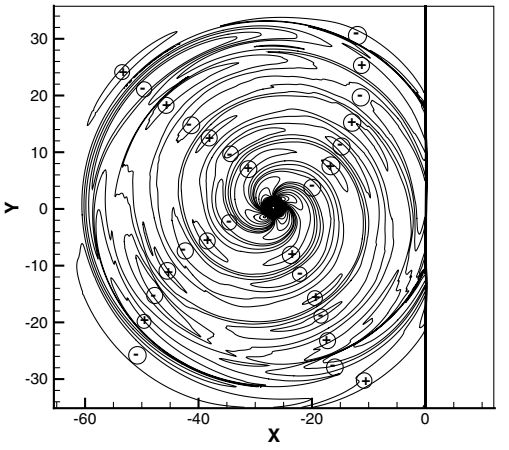

b)

Fig. 6 Sound pressure field a) $t = 20$ showing the four sound waves and b) $t = 34$ showing the seven sound waves.

domain size and simulation time in [4] could result in additional sound waves for higher values of M_v (as in case A) than considered there.

In the present work, test cases in Table 1 are solved on a domain measuring 80×80. It may be noted that case A was the strongest interaction solved for in [7], but on a much smaller domain. Two uniform discretizations corresponding to 640×640 and 1050×1050 grid points are employed along with seventh- and ninth-order spatial accuracy. Results obtained for case A on both discretizations using seventh- or ninth-order schemes are visually identical. This was also true for similar exercises carried out in previous works [3,7]. The uniform grid spacing of 0.076 (for the finer grid) is larger than that used in [3,4,7]. However, the numerical scheme used in the present work is of a higher spatial accuracy than that previously used for similar simulations in literature.

III. Numerical Results: Case A

Results are presented for case A on the finer discretization consisting of 1050×1050 grid points using seventh- and ninth-order WENO schemes. Initially, results are presented at $t = 16$. This was the total simulation time in [7], and a total of three sound waves were observed. Figure 3 compares radial and circumferential distribution of sound pressure for the present case with that in [7]. Peaks R and R' (R1 and R7 in [7]) in Fig. 3a are attributed to secondary shock structures. As in [7], R is located between the precursor and the second sound wave and R' is located between the second and third sound waves. There is a reasonable match between the two results. Intermediate results obtained in the form of shadowgraphs bring out the multistage feature of the shock–vortex interaction. These are seen to be identical to that in [7] and are not presented here.

Results in the form of radial and circumferential variation of sound pressure are presented at $t = 20$ in Fig. 4 and $t = 34$ in Fig. 5. At $t = 20$, a fourth sound wave is seen to develop. Up to seven sound waves can be seen in the computational and physical domain at $t = 34$. The sound waves tend to be quadrupolar in nature and successively out of phase, as is the case with the three sound waves arising out of the primary or first-stage interaction. Figures 6a and 6b, respectively, show the out-of-phase character of successive quadrupolar sound waves in terms of pressure field (Δp) contours at $t = 20$ and 34. Four sound waves can again be discerned at $t = 20$ in Fig. 6a, and seven sound waves can be discerned at $t = 34$ in Fig. 6b. Compression ($\Delta p > 0$) and rarefaction ($\Delta p < 0$) regions in the contour plots are, respectively, denoted by $\oplus$ and $\ominus$. The pressure peaks for the seven sound waves captured are plotted against r for ninth- and seventh-order spatially accurate schemes in Figs. 7a and 7b, respectively. The decay in sound pressure tends to be approximately proportional to $r^{-1/2}$ in the far field, as expected for two-dimensional flows.

IV. Numerical Results: Comparisons

The five test cases listed in Table 1 are solved using a ninth-order-accurate WENO scheme on a discretization consisting of 640×640 grid points. As mentioned, results obtained for case A on a 640×640 grid and a 1050×1050 grid using ninth-order spatial accuracy are visually identical. Cases B and C are derived from case A by, respectively, increasing and decreasing M_s while keeping M_v

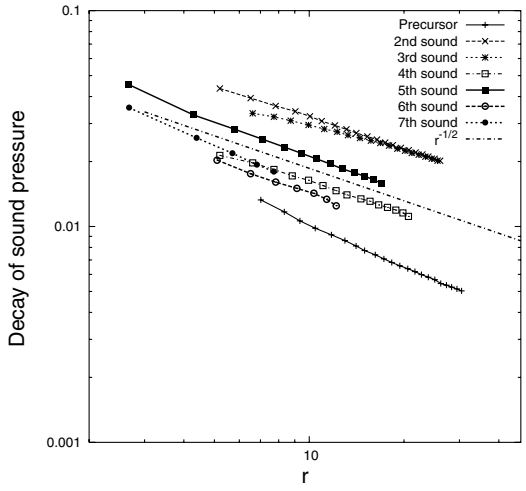

a)

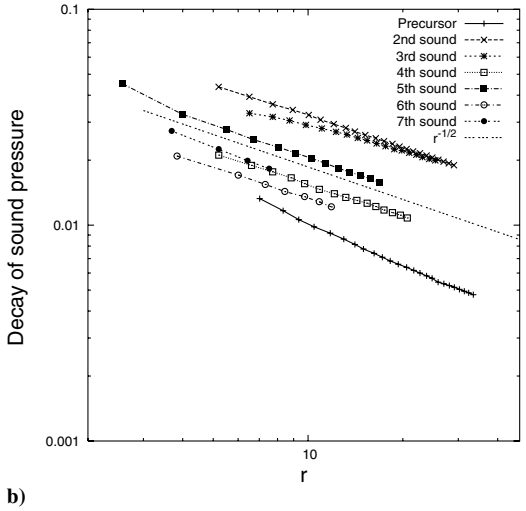

b)

Fig. 7 Decay of peak sound pressure for the seven sound waves: a) ninth-order WENO scheme and b) seventh-order WENO scheme.

constant. This allows us to study the effect of a change in the shock wave Mach number M_s on the acoustic wave generation process. Similarly, cases D and E are derived from case A by varying M_v while keeping M_s constant and trying to capture the effect of M_v in the problem. All test cases are chosen in the range of shock–vortex interactions that exhibit a multistage feature [7].

A. Effect of M_s

The radial distributions for cases A, B, and C are plotted at times $t = 16$, 20, and 34 in Figs. 8a–8c. Decreasing the shock wave Mach number results in weaker secondary shock structures R and R', as can be seen in Fig. 8. Figure 8a shows a decrease in sound pressure with decreasing M_s. Similar observations have been made by Inoue and Hattori [3] for the limited number of sound waves captured in their computations. Figure 8b at $t = 20$ also indicates a varying degree of development for the sound waves as M_s is varied. For the highest value of M_s (case B), a fifth sound wave is seen to form, whereas the fourth sound wave is yet to fully develop for case C. Results at $t = 34$ in Fig. 8c reinforce the effect of M_s on the degree of development of the sound waves generated in the shock–vortex interaction. Case A at $t = 34$ shows seven sound waves in the computational domain. Case B, derived from case A by increasing M_s, shows the presence of eight sound waves at the same time. In contrast, case C with a lower value of M_s shows six sound waves. The eight and six sound waves for cases B and C at $t = 34$ are also shown in the form of sound pressure fields in Figs. 9a and 9b. The pressure peaks for sound waves captured for cases B and C are plotted against r in Figs. 10a and 10b, respectively. The decay in sound pressure is again approximately proportional to $r^{-1/2}$ in the far field.

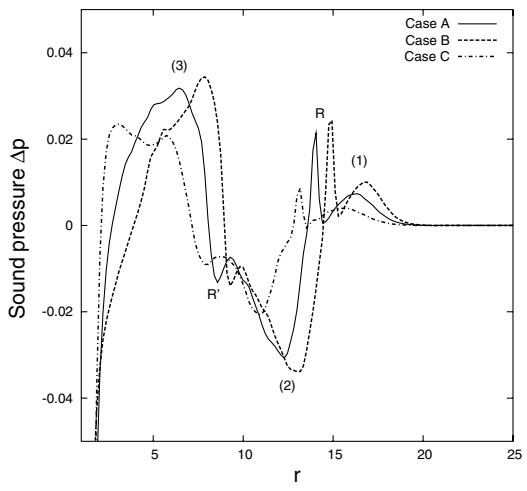

a)

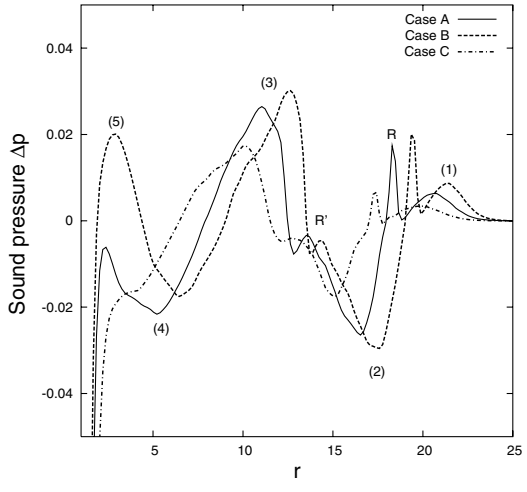

b)

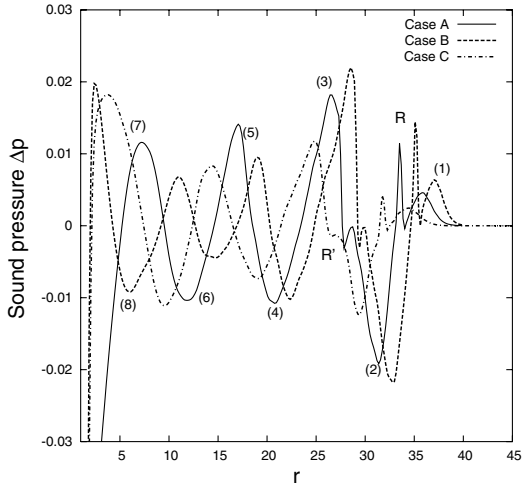

c)

Fig. 8 Effect of shock wave Mach number M_s radial distribution at $\theta = -45$ deg: a) $t = 16$, b) $t = 20$, and c) $t = 34$.

B. Effect of M_v

Figures 11a–11c compare the radial pressure variation for cases A, D, and E. These test cases are meant to bring out the effect of the vortex Mach number M_v on the acoustic wave generation process.

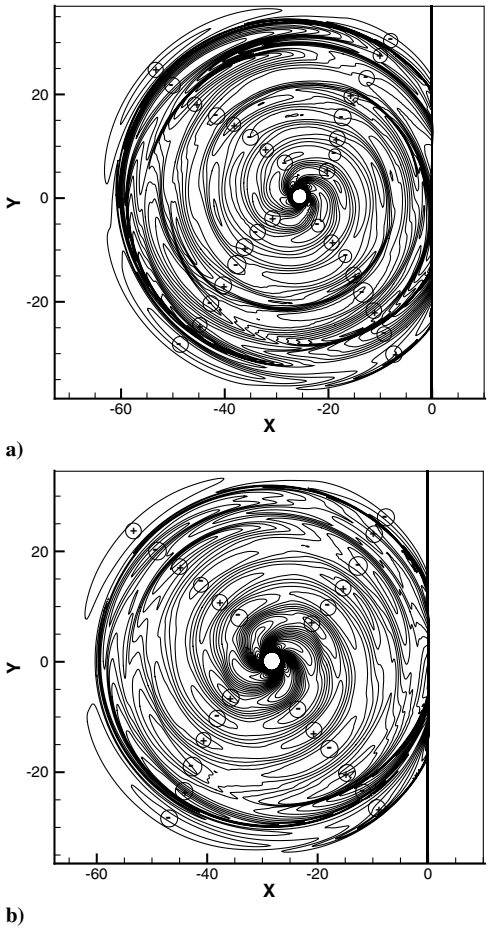

Fig. 9 Sound pressure field $t = 34$: a) case B ($M_s = 1.3$) showing eight sound waves and b) case C ($M_s = 1.1$) showing six sound waves.

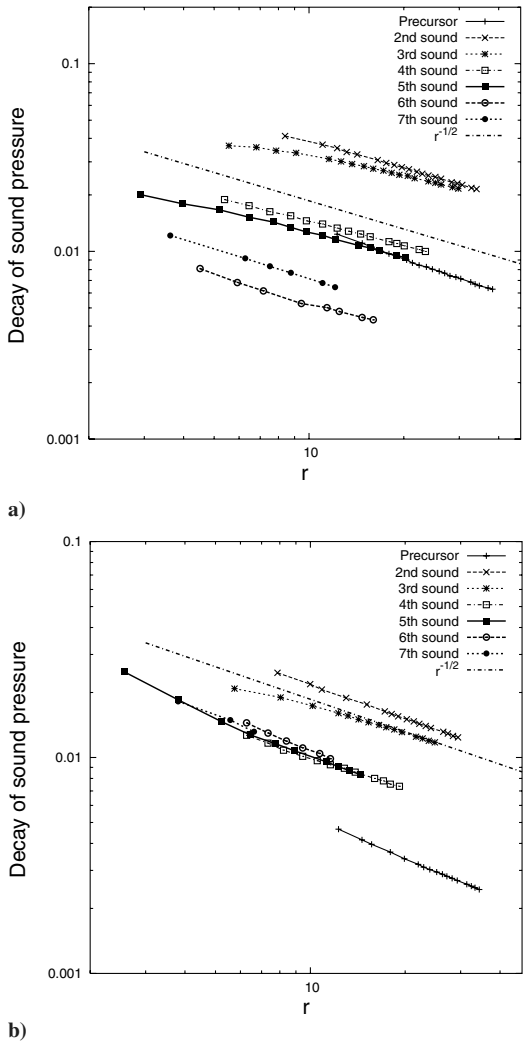

Fig. 10 Decay of peak sound pressure: a) case B ($M_s = 1.3$) and b) case C ($M_s = 1.1$).

Sound waves tend to show a similar degree of development in time with varying M_v. There is an increase in the magnitude of sound pressure with increasing M_v. Again, similar observations regarding the influence of M_v on sound pressure have been made by Inoue and Hattori [3] in their numerical simulations involving a relatively weaker vortex. Changes in M_v also have an effect on the strength of secondary shocks R and R'. An additional pressure peak is also seen to develop between the third and the fourth sound waves for the lowest value of M_v considered (case E).

V. Generation of Additional Sound Waves

Additional sound waves generated in present numerical simulations are discussed with reference to case A. Sound waves in excess of the usual three reported in literature for shock–vortex interactions involving an isolated vortex are referred to as additional sound waves. Figures 12a–12c show the computed flowfield for case A in terms of numerical shadowgraphs (contours of $\nabla^2\rho$) at $t = 8$, 12, and 20. The computed flowfields at $t = 8$ and 12 show secondary and tertiary interactions, with reflected shocks and shocklets interacting with the deformed vortex. Similar shadowgraphs for the same time instants are presented in [7]. The multistage feature of the interaction dies down in time, with increasing separation between shock wave and the vortex. Secondary and tertiary interactions are completely absent for case A by $t = 20$, as seen in Fig. 12c. Acoustic waves still continue to be generated, as evident by the presence of four sound waves at $t = 20$ in Fig. 4 and seven sound waves at $t = 34$ in Fig. 5. This indicates that additional acoustic waves captured in present simulations are not generated due to multistage nature of the shock–vortex interaction process in which additional shock structures interact with the deformed vortex.

The additional sound waves generated in present simulations are also centered around the vortex and propagate radially outward. As opposed to sound waves generated in the primary shock–vortex interaction, additional sound waves do not have embedded pressure peaks due to secondary shock structures. This can be seen by contrasting the first three sound waves in Fig. 5 with the fourth, fifth, sixth, and seventh sound waves. The first three sound waves in Fig. 5 are generated due to the primary shock–vortex interaction and the rest represent additional sound waves for case A at $t = 34$. The increasing separation of the shock wave and the vortex, the absence of secondary and tertiary interactions at larger times ($t > \sim 16$), and the preceding observations suggest the vortex to be the source of additional sound waves captured in present simulations.

Vorticity contours are plotted between $t = 12$ and 34 in Figs. 13a–13f. As reported in literature [5–8,17], the initially circular vortex is compressed to an elliptical shape due to its interaction with the shock wave, as seen in Figs. 13b–13f. Figure 13a shows the deformed and relatively irregular shaped vortex at $t = 12$; almost identical vorticity contours for the same time instant are also presented in [7]. Secondary and tertiary interactions are still active at $t = 12$, though the vortex has well passed the incident shock wave. This can seen in the shadowgraph for the computed flowfield at $t = 12$ in Fig. 12b. Thereafter, the vortex is gradually compressed to an elliptical shape. In shock–vortex interactions involving a relatively weaker vortex, the initially circular vortex is compressed to an elliptical shape as soon as it passes the incident shock wave [7,8]. A strong vortex in the present context has $M_v \geq \sim 0.7$ (for present values of M_s) and exhibits features of multistage shock–vortex interaction [7]. Figures 13b–13f show the elliptical vortex rotating counterclockwise as it convects downstream. Successive vorticity plots in Figs. 13b–

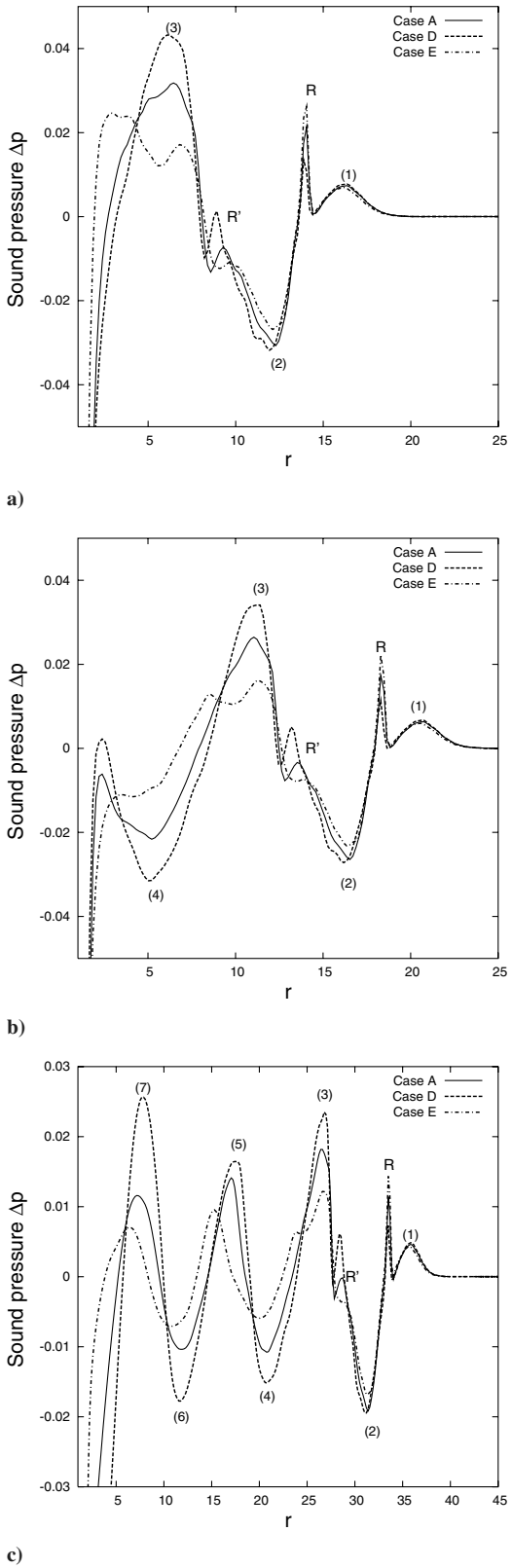

Fig. 11 Effect of the vortex Mach number M_v radial distribution at $\theta = -45$ deg: a) $t = 16$, b) $t = 20$, and c) $t = 34$.

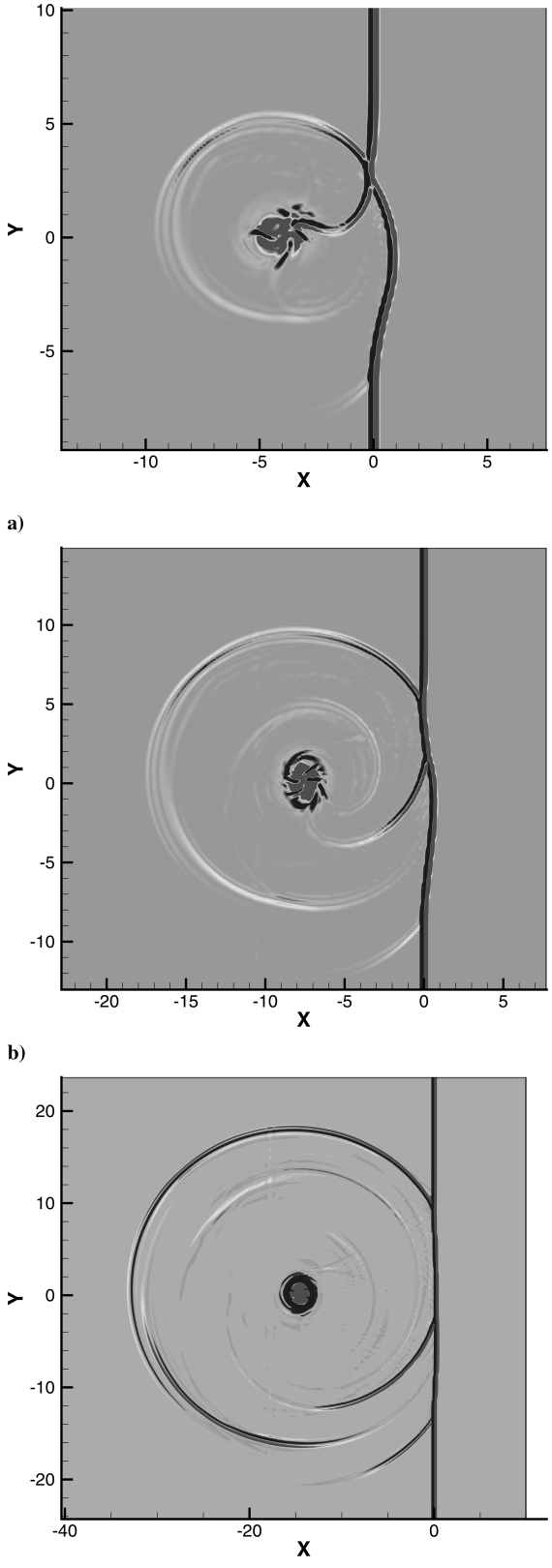

Fig. 12 Shadowgraphs for case A: a) $t = 8$, b) $t = 12$, and c) $t = 20$.

13e show a vortex rotation of approximately $\pi/2$ rad, indicating an almost constant angular velocity. Acoustic wave generation from the rotating elliptical vortex resembles that from a rotating quadrupole, as seen in the sound pressure fields in Fig. 6. Between $t = 16$ and 34, four additional sound waves are generated for the interaction in case A, as seen from Figs. 3 and 5. This period also corresponds to an approximately 2π rotation for the vortex as it convects downstream. This can be seen from the vorticity contour plots in Fig. 13b–13f. Thus, one complete revolution of the elliptical vortex results in the generation of four quadrupolar acoustic waves with successive waves of opposite polarity. Ellzey and Henneke [8] have shown that the quadrupolar acoustic wave in shock–vortex interactions can be re-created using a single elliptical vortex. Acoustic radiation from the

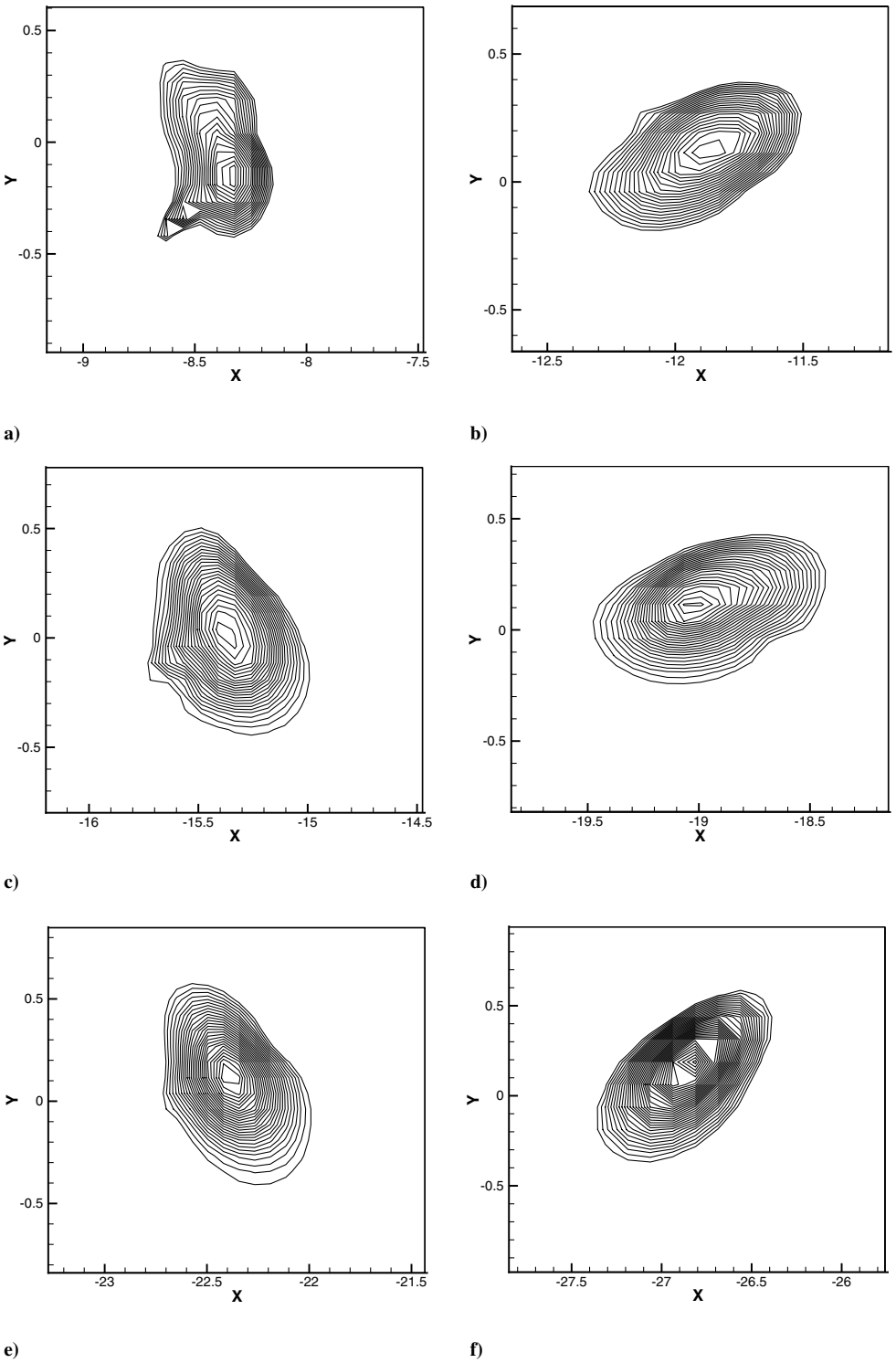

Fig. 13 Vorticity contours for case A: a) $t = 12$, b) $t = 16$, c) $t = 20$, d) $t = 24$, e) $t = 28$, and f) $t = 34$.

rotating elliptical vortex leads to the generation of multiple acoustic waves, quadrupolar in nature and successively out of phase.

The preceding results are also compared with that for an incident shock wave interacting with a relatively weaker vortex. The incident shock wave has $M_s = 1.2$ (as in case A), but the vortex is relatively weaker with $M_v = 0.5$. In the present work, this is referred to as the weak interaction. This interaction has been analyzed in detail in [4], in which computations in a similarly sized domain until $t = 40$ showed the presence of only three sound waves. Multistage features are also absent in the weak interaction [7]. Vorticity contours in Figs. 14a–14d show the weak vortex between $t = 5$ and 25, following the shock–vortex interaction. The computed flowfield at $t = 15$ is shown in terms of a numerical shadowgraph in Fig. 15. There is significant rotation for the elliptically compressed vortex only until $t \sim 15$, with the elliptical vortex rotating by approximately 1.5π rad between $t = 5$ and 15. Intermediate stages are not shown due to space constraints. The elliptical vortex is seen to relax to an almost circular shape by $t = 25$. Computations in [4] confirm the presence of the third sound wave by $t = 20$, after which no additional sound waves are generated. This is also verified in the present work. It is interesting to note that the appearance of the third sound wave in the weak interaction seems to coincide with the end of significant rotation of the elliptical vortex. Thus, absence of extra sound waves in a weak interaction can be attributed to the lack of significant

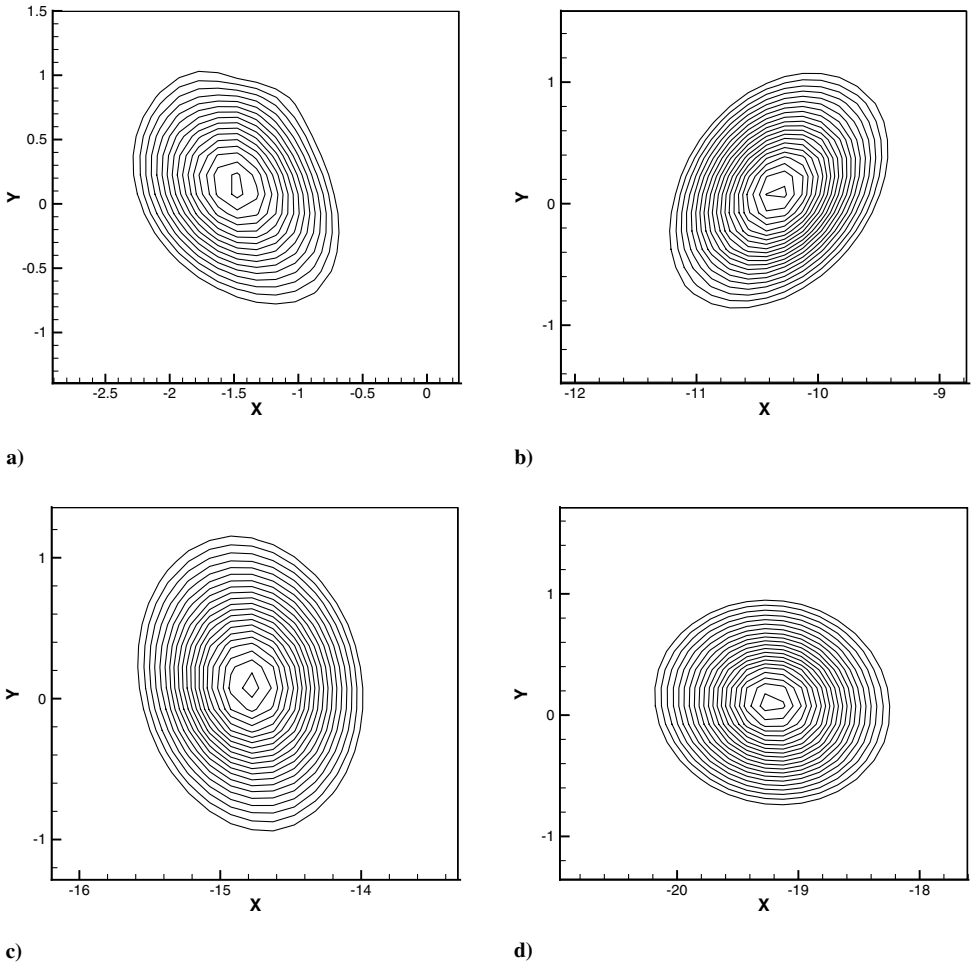

Fig. 14 Vorticity contours for weak interaction: a) $t = 5$, b) $t = 15$, c) $t = 20$, and d) $t = 25$.

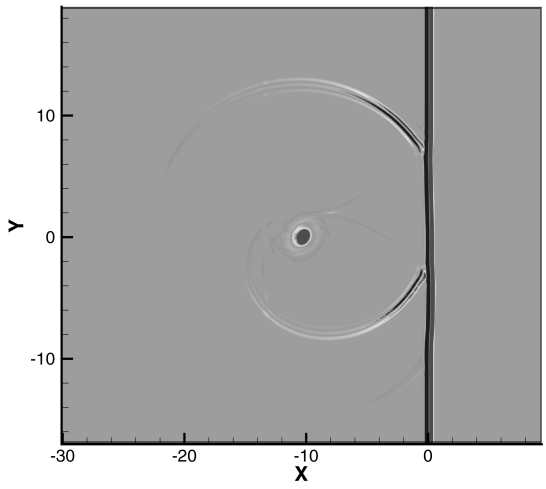

Fig. 15 Shadowgraph of weak interaction $t = 15$.

rotation for the elliptical vortex following the shock–vortex interaction. In contrast, acoustic radiation from the still rotating elliptical vortex leads to generation of multiple acoustic waves for interactions involving a strong vortex. In literature, similar sound generation from a rotating elliptical vortex is observed in the well-known case of a single Kirchoff vortex. The Kirchoff vortex is a two-dimensional elliptical patch of constant vorticity in irrotational flow. It rotates with a constant angular velocity about the origin without change of shape. Sound generation from a single Kirchoff vortex for low and moderate aspect ratios have been numerically simulated by solving the two-dimensional compressible Euler [18] and Navier–Stokes equations [19]. The quadrupolar acoustic waves captured [18,19] are very similar to additional sound waves generated due to the rotating elliptical vortex in the present work and resemble that radiated from a rotating quadrupole.

VI. Conclusions

Shock–vortex interactions involving a strong vortex are numerically simulated using a ninth-order spatially accurate WENO scheme in a relatively large computational domain for long simulation times. Multiple quadrupolar sound waves, which tend to be successively out of phase, are captured. The maximum number of sound waves captured in such simulations have previously been limited to three in literature. Computations rule out the possibility of additional acoustic waves being generated due to multistage nature of shock–vortex interactions. Additional acoustic waves captured in present simulations are attributed to that radiated from the rotating elliptical vortex following the interaction between an incident planar shock wave and a circular vortex. Most numerical studies on shock–vortex interactions in literature involving a strong vortex have been for shorter simulation times. The sound generation mechanism for the maximum three acoustic waves captured in such simulations is thought to be shock distortion and vortex compression induced by the incident shock wave. The present work indicates a different mechanism of sound generation for interactions involving a strong vortex at later times in the form of acoustic radiation from the rotating elliptical vortex. The overall symmetry in the successive multiple quadrupolar sound waves captured in the present numerical simulations further suggests acoustic radiation from the rotating

elliptical vortex to be the dominant mechanism for sound generation in shock–vortex interactions.

Acknowledgment

This work was supported partially by Korea Research Foundation grant KRF-2005-005-J09901. The authors wish to thank Debojyoti Ghosh, former graduate student at the Department of Aerospace Engineering, Indian Institute of Technology, Bombay, for help with computations.

References

[1] Ribner, H. S., "Cylindrical Sound Wave Generated by Shock–Vortex Interaction," *AIAA Journal*, Vol. 23, No. 11, 1985, pp. 1708–1715. doi:10.2514/3.9155

[2] Ellzey, J. L., Henneke, M. R., Picone, J. M., and Oran, E. S., "The Interaction of a Shock with a Vortex: Shock Distortion and the Production of Acoustic Waves," *Physics of Fluids*, Vol. 7, No. 1, 1995, pp. 172–184. doi:10.1063/1.868738

[3] Inoue, O., and Hattori, Y., " Sound generation by Shock Vortex Interactions," *Journal of Fluid Mechanics*, Vol. 380, 1999, pp. 81–116. doi:10.1017/S0022112098003565

[4] Inoue, O., "Propagation of Sound Generated by Weak Shock–Vortex Interaction," *Physics of Fluids* Vol. 12, No. 5, 2000, pp. 1258–1261. doi:10.1063/1.870378

[5] Grasso, F., and Pirozzoli, S., "Shock-Wave-Vortex Interactions: Shock and Vortex Deformations and Sound Production," *Theoretical and Computational Fluid Dynamics*, Vol. 13, No. 6, 2000, pp. 421–456. doi:10.1007/s001620050121

[6] Rault, A., Chiavassa, G., and Donat, R., "Shock Wave Interactions at High Mach Numbers," *Journal of Scientific Computing*, Vol. 19, Nos. 1–3, 2003, pp. 343–371. doi:10.1023/A:1025316311633.

[7] Zhang, S., Zhang, Y. T., and Shu, C. W., "Multistage Interaction of a Shock Wave and a Strong Vortex," *Physics of Fluids* Vol. 17, No. 11, 2005, Paper 116101. doi:10.1063/1.2084233

[8] Ellzey, J. L., and Henneke, M. R., "The Shock–Vortex Interaction: The Origin of the Acoustic Wave," *Fluid Dynamics Research*, Vol. 21, No. 3, 1997, pp. 171–184. doi:10.1016/S0169-5983(97)00006-3

[9] Jiang, G.- S., and Shu, C.- W., "Efficient Implementation of Weighted ENO Schemes," *Journal of Computational Physics*, Vol. 126, No. 1, 1996, pp. 202–228. doi:10.1006/jcph.1996.0130

[10] Balsara, D. S., and Shu, C.- W., "Monotonicity Preserving Weighted Essentially Nonoscillatory Schemes with Increasingly Higher Orders of Accuracy," *Journal of Computational Physics*, Vol. 160, No. 2, 2000, pp. 405–452. doi:10.1006/jcph.2000.6443

[11] Harten, A., and Osher, S., "Uniformly Higher-Order Accurate Nonoscillatory Schemes, 1," *SIAM Journal on Numerical Analysis*, Vol. 24, No. 2, 1987, pp. 279–309. doi:10.1137/0724022

[12] Harten, A., Engquist, B., Osher, S., and Chakravarthy, S., "Uniformly Higher Order Accurate Nonoscillatory Schemes, 3," *Journal of Computational Physics*, Vol. 71, No. 2, 1987, pp. 231–303. doi:10.1016/0021-9991(87)90031-3

[13] Shu, C.-W., "Preface to the Republication of 'Uniformly Higher Order Accurate Nonoscillatory Schemes, 3' by Harten, Engquist, Osher, and Chakravarthy," *Journal of Computational Physics*, Vol. 131, No. 1, 1997, pp. 1–2. doi:10.1006/jcph.1996.5630

[14] Erlebacher, G., Hussaini, M. Y., and Shu, C.- W., " Interaction of a Shock with a Longitudinal Vortex," *Journal of Fluid Mechanics*, Vol. 337, Feb. 1997, pp. 129–153. doi:10.1017/S0022112096004880

[15] Chatterjee, A., "Shock Wave Deformation in Shock–Vortex Interactions," *Shock Waves*, Vol. 9, No. 2, 1999, pp. 95–105. doi:10.1007/s001930050144

[16] Jing, S., Zhang, Y- T., and Shu, C.- W., "Resolution of High Order WENO Schemes for Complicated Flow Structures," *Journal of Computational Physics*, Vol. 186, No. 2, 2003, pp. 690–696. doi:10.1016/S0021-9991(03)00094-9

[17] Dosanjh, D. S., and Weeks, T. M., "Interaction of a Starting Vortex as Well as a Vortex Street with a Traveling Shock Wave," *AIAA Journal*, Vol. 3, No. 2, 1965, pp. 216–223. doi:10.2514/3.2833

[18] Muller, B., and Yee, H. C., "Higher Order Numerical Simulation of Sound Generated by Kirchoff Vortex," *Computing and Visualization in Science*, Vol. 4, No. 3, 2002, pp. 197–204. doi:10.1007/s007910100072

[19] Barre, S., Bogey, C., and Bailly, C., "Direct Simulation of Isolated Elliptic Vortices and of Their Radiated Noise," *Theoretical and Computational Fluid Dynamics*, Vol. 22, No. 1, 2008, pp. 65–82. doi:10.1007/s00162-007-0066-x

K. Powell
Associate Editor